Multi-site electrocatalysts for hydrogen evolution in neutral media by destabilization of water molecules

Cao-Thang Dinh, Ankit Jain, F. Pelayo García de Arquer, Phil De Luna, Jun Li, Ning Wang, Xueli Zheng, Jun Cai, Benjamin Z. Gregory, Oleksandr Voznyy, Bo Zhang, Min Liu, David Sinton, Ethan J. Crumlin, and Edward H. Sargent

UNIVERSITY OF TORONTO LIBRARIES

Multi-site electrocatalysts for hydrogen evolution in neutral media by destabilization of water molecules

Cao-Thang Dinh[†,1], Ankit Jain[†,1], F. Pelayo García de Arquer[†,1], Phil De Luna[1], Jun Li[1,3], Ning Wang[1], Xueli Zheng[1], Jun Cai[2], Benjamin Z. Gregory[2], Oleksandr Voznyy[1], Bo Zhang[1], Min Liu[1], David Sinton[3], Ethan J. Crumlin[2], Edward H. Sargent[1,*]

[1]*Department of Electrical and Computer Engineering, University of Toronto, 35 St George Street, Toronto, Ontario M5S 1A4, Canada*

[2]*Advanced Light Source, Lawrence Berkeley National Laboratory, One Cyclotron Road, Berkeley, California 94720, USA*

[3]*Department of Mechanical and Industrial Engineering, University of Toronto, 5 King's College Rd., Toronto, Ontario M5S 3G8, Canada*

[†] These authors contributed equally to this work.
*corresponding author: ted.sargent@utoronto.ca

High-performance hydrogen evolution reaction (HER) catalysts are compelling for the conversion of renewable electricity to fuels and feedstocks. The best HER catalysts rely on the use of platinum and show the highest performance in acidic media. Efficient HER catalysts based on inexpensive and Earth-abundant elements that operate in neutral (hence biocompatible) media could enable low-cost direct seawater splitting and the realization of bio-upgraded chemical fuels. In the challenging neutral-pH environment, water splitting is a multistep reaction. Here we design a new HER catalyst that operates efficiently in neutral media. Our strategy employs a combination of sites with a large contrast between hydrogen (Ni) and hydroxyl (CrO$_x$) binding energies, which are doped on a Cu surface with a weak hydrogen binding energy to accelerate water dissociation and promote hydride coupling. The resulting catalysts exhibit a 48 mV overpotential at a current density of 10 mA·cm^{-2} in a pH 7 buffer electrolyte. These findings suggest design principles for inexpensive, efficient and biocompatible catalytic systems.

Hydrogen is of central importance in key industrial processes such as oil refining, and is widely used as a feedstock in the production of various chemicals such as ammonia and methanol [1-4]. Its compelling properties as an energy carrier make H_2, synthesized electrochemically or photoelectrochemically from renewable sources, an attractive alternative to fossil fuels.

In electrocatalytic water splitting for H_2 production, HER can be performed in acidic, basic or neutral media. Among these conditions, HER in basic and neutral media are the most challenging, as their kinetics are slowed by the requirement of an additional water dissociation step [5-7]. The most active HER catalyst in acidic media, platinum (Pt), shows 2 to 3 orders of magnitude lower activity when operated in neutral media [8].

If HER could be achieved efficiently in neutral environments, it would be of interest in the large-scale production of H_2. Neutral HER allows the application of active catalysts based on Earth-abundant transition metals that are typically unstable in acidic media. This would have the benefit of avoiding reliance on scarce and expensive noble metals. Additionally, electrolysers operating in neutral media can potentially enable the direct use of saltwater without the requirement of desalination for pH maintenance. This increases the feasibility of splitting seawater, the most abundant water source, in H_2 production.

Neutral HER can also be combined with bio-processes for the production of solar fuels [9,10]. As a feedstock, hydrogen can be used to convert carbon dioxide to value-added chemicals, representing a potential solution for the integrated and efficient conversion and storage of renewable energy [11-13]. However, the integration of hydrogen-producing systems with hydrogen-powered bio-upgrading systems requires that the operating conditions for HER be compatible with the environment needed by microorganisms involved in the upgrade of CO_2 to chemical fuels, and these generally rely on neutral pH.

Previous studies used both experiments and theory to posit the key steps in water dissociation in neutral media. These begin with ($H_2O+e^-+M \rightarrow M-H_{ad}+OH^-$) and are followed by either the electrochemical Heyrovsky step ($H_2O+M-H_{ad}+e- \rightarrow M+H_2+OH^-$) or the chemical Tafel recombination step ($2H_{ad} \rightarrow H_2$) [5,7].

Prior approaches to improve the kinetics of water dissociation in neutral media have focused on either surface texturing of the catalyst; or on the incorporation of additional water dissociation

compounds such as metal hydroxides within the catalyst [8,14-18]. Surface texturing creates surface active sites such as edges, corners, and grain boundaries that accelerate the rate of the water dissociation reaction. Metal hydroxide (M-OH) doping promotes water dissociation, providing a proton at the metal/hydroxide interface which then combines with a second proton to generate H_2 on the metal surface[19]. These approaches have improved the activity of metal catalysts in basic media; with the water dissociation enhancement based principally on the optimization of the M-OH interaction. They have relied on the use of rare metals such as Pt that exhibit an optimum hydrogen binding energy (HBE) for hydrogen generation[5,8].

A general design principle for active HER catalysts in neutral water that includes inexpensive and Earth-abundant elements and strategies for accelerating water dissociation beyond M-OH optimization remains to be reported.

Here we offer design principles for highly active HER catalysts in neutral media. Specifically, we propose an anisotropic surface doping strategy which, in contrast with prior approaches, employs the combination of a metal with a strong HBE and a metal oxide with a strong OH binding energy to accelerate the water dissociation. These two species are doped on a supporting metal surface having a weak HBE to further optimize the HBE for H_2 evolution. The approach is designed to promote water dissociation due to the high contrast between the strong HBE of one metal and the high OH binding energy of the oxide. It thereby decouples the optimization of water dissociation and hydrogen evolution, allowing incorporation of catalytic sites exhibiting superior H-H coupling. Using these design principles, we demonstrate $CrO_x/Ni/Cu$ multi-site catalysts in which CrO_x strongly binds OH, and Ni strongly binds H, accelerating water dissociation on Cu surface and thus achieving rapid H_2 generation. These catalysts exhibit high performance for HER with an overpotential of only 48 mV at a current density of 10 mA cm^{-2} in a pH 7 buffer electrolyte.

Asymmetric doping and O-OH bond destabilization

We hypothesized that the dissociation of water in neutral media would be accelerated if the H-OH bond was destabilized. This could be achieved if the surface of the catalyst consisted of two distinct sites, one that interacted strongly with H, the other with OH (Fig. 1a). We devised a system comprised of a metallic copper catalyst modified with metal oxide clusters, one designed with

distinct elements featuring widely different binding energies for H and OH: Cu sites offer preferential binding for H, whereas metal oxides promote OH adsorption [20].

We began by identifying the effect of incorporating different metal oxide clusters (MO_x, M = Cr, Al, Fe, Co, Ti, W) on the HER activity of Cu catalysts. To achieve this goal, we deposited MO_x on the surface of a polished Cu foil by thermally decomposing nitrate salts of the corresponding metal at 400°C in nitrogen atmosphere to form MO_x/Cu samples. This method enables precise control over the loading and composition of the samples. The metal oxide loading of all samples was kept at 0.02 mg of metal per square centimeter. X-ray photoelectron spectroscopy analysis of the Cu surface before and after MO_x deposition reveals that the metal oxide covers about 50% of total surface area (Supplementary Figure 1).

HER activity testing of MO_x/Cu catalysts was carried out using a three-electrode electrochemical cell in a 1 M KPi buffer solution (pH 7). The deposition of the various metal oxides was found to improve Cu HER activity except for MnO_x, which showed a similar HER activity (Fig. 1b, and Supplementary Figure 2). In particular, CrO_x/Cu showed a significant increase in activity, with a current density of 3.3 mA cm^{-2} at -0.2 V *vs.* RHE. This is more than an order of magnitude higher than that of pure Cu (0.3 mA cm^{-2} at -0.2 V *vs.* RHE) (Fig. 1c). To exclude the effect of active surface area modification caused by the addition of metal oxides, we measured the electrochemically active surface areas (ECSA) of the Cu and CrO_x/Cu samples using double layer capacitance. We found that the capacitance of CrO_x/Cu is only 1.6 times higher compared to that of Cu (Supplementary Figure 3). The superior HER activity of CrO_x/Cu is therefore stemming from its intrinsic activity.

To assess the activity of CrO_x alone for the HER reaction, we deposited CrO_x on a carbon substrate with a similar mass loading. HER testing in similar conditions to those of CrO_x/Cu reveals a negligible activity, with a current density of 0.1 mA cm^{-2} at -0.2 V *vs.* RHE. This confirms that CrO_x itself is not an active material for HER. We carried out additional control experiments to verify the role CrO_x has in HER performance, and removed the CrO_x layer in the CrO_x/Cu system by immersing the sample in an HCl solution (1 M). The HER activity of CrO_x/Cu is significantly decreased after CrO_x removal (Supplementary Figure 4). This indicates the synergistic role of CrO_x on the high HER activity of CrO_x/Cu catalysts.

We then sought to further improve the CrO_x/Cu catalyst by doping the Cu surface with Ni. We chose Ni as it binds to H more strongly than Cu, thereby enhancing the H binding energy to Cu-Ni sites to favour water dissociation. We prepared Cu-Ni/Cu catalysts by decomposing a mixture of copper and nickel nitrate salts on the surface of the Cu foil. The loading of the catalyst used was 0.1 mg cm^{-2}. The HER activity of a series of Cu-Ni catalysts reveals that two compositions (Cu:Ni molar ratio of 1:2 and 2:1) show substantially improved activity compared to individual Cu and Ni catalysts (Supplementary Figure 5). Specifically, Cu-Ni 1:2 catalyst delivers a current density of 0.9 mA cm^{-2} at -0.2 V vs. RHE. This is 3 and 1.4 times higher than those of Cu and Ni samples respectively (Fig. 1c). When CrO_x was further deposited on the optimum Cu-Ni catalyst (CrO_x/Cu-Ni), a significant improvement in HER activity was found. The CrO_x/Cu-Ni 1:2 catalyst shows a current density of 7 mA cm^{-2} at -0.2 V vs. RHE. This is 20 times higher than those of Cu and Ni, showcasing the synergistic effect of CrO_x and Ni surface doping on HER activity of Cu catalyst.

To assess the effect of CrCuNi configuration on the HER catalytic activity, we explored different ways to deposit each component: depositing CrO_x on the surface of Cu-Ni (CrO_x/Cu-Ni); co-depositing Cr, Ni, and Cu ($CrCuNiO_x$); and depositing Cu-Ni on the surface of CrO_x (Cu-Ni/CrO_x). We found that the order of CrO_x and Cu-Ni deposition significantly affects HER performance of the CrCuNi catalysts (Fig. 1c). CrO_x/Cu-Ni, with a current density of 7.7 mA cm^{-2} is 1.5 and 5 times more active than $CrCuNiO_x$ and Cu-Ni/CrO_x, respectively. We measured the ECSA of the samples to study the effect of the deposition sequence. We found that CrO_x/Cu-Ni catalyst exhibited a 2.2 times higher ECSA compared to that of Cu-Ni/CrO_x (Supplementary Figure 6). This result shows that CrO_x maximizes its positive effect on HER when it is evenly dispersed on the surface of the active layer (i.e. Cu-Ni).

Morphochemical characterization

To shed light on the microstructure of CrO_x/Cu-Ni catalysts, we carried out X-ray absorption fine structure (XAFS) spectroscopy at the K-edges of Cr, Ni and Cu with electron transitions from 1s to 4p states to examine their respective local structures. While the Cr foil exhibits a broad metallic spectral pattern (Fig. 2a) at the Cr K-edge X-ray absorption near-edge structure (XANES), chromium-based compounds (CrO_x/Ni, CrO_x/Cu and CrO_x/Cu-Ni, Fig. 2a) show well-resolved XANES characteristics with absorption thresholds blue-shifted and white-line intensity enhanced, especially the cases of CrNi and CuCrNi. These data confirm that the chromium in the samples

exists in the form of oxide. The absence of a well-defined pre-edge peak between 5985 and 6000 eV among all Cr-based compounds indicates that chromium exists in a trivalent form (Cr_2O_3)[21]. Consistent results are seen in the Extended X-ray Absorption Fine Structure (EXAFS) (Fig. 2d). Fourier transforms of the Cr K-edge EXAFS spectra of CrO_x/Ni, CrO_x/Cu and CrO_x/Cu-Ni show two distinct peaks at ~1.5 and ~2.5 Å, corresponding to Cr-O and Cr-M (M: Cr, Ni and/or Cu) distances, respectively, in a chromium oxide phase. These data further confirm the oxide nature of chromium in the designed catalysts.

The presence of CrO_x strongly affects the local structure of Ni and Cu. With respect to Ni, the changes of spectral features between Ni foil and Ni compounds are similar to the case of Cr, where the absorption onsets and white-line intensities of Ni compounds are both increased compared to that of Ni foil at their Ni K-edge XANES. This indicates that Ni species are oxidized in these compound materials, especially those with Cr included. EXAFS spectra of CrO_x/Ni and CrO_x/Cu-Ni show the presence of Ni in an oxide phase, as evidenced by the two peaks at ~1.6 and ~2.5 Å, attributable to Ni-O and Ni-M (M: Ni, Cu, and/or Cr) bonds[22]. In the case of Cu, XANES and EXAFS data (Fig. 2c and f) reveal a dominant metallic Cu phase in all samples. The slight increase of absorption onset and white-line intensity in the Cu K-edge XANES spectra of Cu-Ni, CrO_x/Cu and CrO_x/Cu-Ni reveal that Ni and CrO_x induce the formation of a small amount of oxidized Cu[23].

In summary, XAFS results reveal the strong modulating effect of CrO_x on the oxidation state of Cu-Ni, leading to an increased oxidation state of Ni and Cu. This is particularly acute for Ni, whose oxidation state is the most sensitive to the presence of CrO_x, which strongly modulates the Ni local structure to become oxidized.

The morphology of the best-performing CrO_x/Cu-Ni sample was characterized using high-resolution scanning electron microscopy (SEM) (Supplementary Figure 7). It revealed the formation of nanoparticles with sizes of ~10 nm. The chemical nature of the CrO_x/Cu-Ni sample was further confirmed using X-ray photoelectron spectroscopy (XPS) (Supplementary Figure 8). We found that Cu is dominated by its metallic Cu^0 phase, while Cr remains as Cr^{3+} in the as-synthesized samples. Ni, on the other hand, exists as NiO, $Ni(OH)_2$ and metallic Ni.

We then performed ambient pressure XPS (AP-XPS)[24] to investigate the adsorption and dissociation of water on CrO_x/Cu-Ni. Fig. 3a shows the curve-fitting of the O 1s XPS spectra for

CrO$_x$/Cu-Ni under ultra-high vacuum (UHV) and under a water pressure of 100 mTorr. The observation of chemisorbed H$_2$O and the increase in OH on the surface in the presence of water clearly indicates water dissociation on CrO$_x$/Cu-Ni sample. We observe a significant change in the Ni 3s XPS spectra for CrO$_x$/Cu-Ni under UHV and 100 mTorr water pressure (Fig. 3b and Supplementary Table 1). Specifically, more than 50 % of metallic Ni was converted to Ni(OH) in the presence of water. This trend is distinct from that exhibited by control Cu-Ni samples, where only NiO was converted to Ni(OH) when exposed to water vapour (Supplementary Figure 9). These results indicate that the presence of CrO$_x$ may induce the conversion of Ni surface to Ni(OH) under the presence of water, in this way enhancing the water dissociation of the Ni surface. We then compared the Ni 3s XPS spectra of CrO$_x$/Cu-Ni and Cu-Ni under UHV and found that more than 40 % of Ni surface is in the form of Ni(OH)$_2$. For Cu-Ni samples this is only 12% despite the similar sample preparation procedure (Supplementary Table 1). This further confirms that the effect CrO$_x$ is to induce water dissociation on CrO$_x$/Cu-Ni samples, leading to a large amount of Ni(OH)$_2$ on its surface.

Computational modeling and catalyst design principles

To understand the origin of CrO$_x$/Cu-Ni high catalytic activity, we performed density functional theory (DFT) calculations. We considered four different surfaces: Cu; Ni-doped Cu; Cr$_2$O$_3$ deposited on Cu; and Cr$_2$O$_3$ deposited on Ni-doped Cu (Fig. 4). We calculated the reaction barrier for water splitting of the Volmer and Tafel steps which involves the dissociation of water and the coupling of H to H$_2$, respectively. These reaction steps depend on how H$_2$O, H and OH bond to the surface of the catalysts. We found that both H$_2$O and H bind weakly to the Cu surface, leading to a large kinetic barrier for the water dissociation step (step 1-3, Fig. 4). While Ni doping of Cu surface only helps stabilize H, Cr$_2$O$_3$ facilitates the adsorption of H$_2$O and OH species (see Supplementary Table 2 for binging energies of H, OH, and H$_2$O on four surfaces). As a result, while the presence of Cr$_2$O$_3$ does not help improve the stability of dissociated H$_2$O (Fig. 4, state 3), the stability is greatly enhanced on the Ni-doped Cu surface. For the hybrid catalyst, with both Ni doping and Cr$_2$O$_3$ deposition, we found that the change in energy for H$_2$O splitting is close to zero ($\Delta E_{3-1} \approx -0.01$ eV). This is in stark contrast to Ni-doped copper, which showcases a preferential binding for H, causing ΔE_{3-1} to be -0.89 eV.

We then calculated the energy barriers (ΔE_{2-1} in Fig. 4) for the decomposition of H_2O into H and OH on four different surfaces and found the minimum barrier in case of hybrid catalyst. The energy required to remove adsorbed H from the reaction site (ΔE_{4-3} in Fig. 4) was found similar for Ni-doped and hybrid catalysts. From the DFT results, the determining step for H_2 generation in neutral media on Cu based catalyst found to be the water dissociation, which is significantly accelerated for certain Cu, Ni and CrO_x configurations.

Neutral-HER electrocatalysts with high activity

Once we found the design guidelines and optimum composition structure of the most active Cr-Cu-Ni hybrid catalyst, we sought to implement this surface in a highly porous CrO_x/Cu-Ni catalyst to increase the active surface area. First, we grew CuO nanowires on a copper foam using a thermal treatment method (see Methods) to form a 3D CuO nanowire structure (Fig. 5a). We then subsequently deposited Ni and CrO_x on the 3D CuO nanowire scaffold. The resulting CrO_x/Cu-Ni catalyst consists of long nanowires (~3 μm) with a diameter of ~1 μm that form a 3D nanowire network (Fig. 5 b-c). High magnification images reveal the presence of small nanoparticles (10 nm) on the surface of the nanowire. Elemental mapping obtained by energy dispersive X-ray spectroscopy shows the homogeneous distribution of Cr, Ni, Cu and O throughout the sample (Fig. 5c). The X-ray diffraction pattern only shows peaks characteristic of Cu metals (Supplementary Figure 10). No peaks of Ni or CrO_x were observed, which indicates the lack of long-range order of these dopants.

We characterized the electrochemical performance of the catalyst using a 1 M KPi buffer electrolyte (pH 7). The CrO_x/Cu-Ni porous catalyst is highly active, and achieves a geometric current density of -10 mA cm^{-2} at the record-low overpotential of 48 mV (Fig. 6). It outperforms highly active Pt catalyst (Pt/C 10%wt) under these conditions, which requires an overpotential of 70 mV to achieve a similar current density (Supplementary Table 3). To the best of our knowledge, the CrO_x/Cu-Ni also shows lower overpotential than other reported HER catalysts operating in neutral media (Supplementary Table 3) such as NiMoS [9], CoP [12], FeP [25]. These catalysts respectively require overpotentials of 200, 180, and 102 mV to achieve a -10 mA cm^{-2} current density. The double layer capacitance, which reveals ECSA, was measured for the CrO_x/Cu-Ni samples to be 65 mF/cm^2 (Supplementary Figure 11). This is comparable to other catalyst systems based on nanosized and hollow structures (Supplementary Table 3). These results indicate that the

higher activity of CrO_x/Cu-Ni catalyst does not stem from a higher surface area, but instead from their superior intrinsic activity.

From the extrapolation of the linear region of a plot of overpotential versus log J, we obtained Tafel slopes of 64, and 81, per decade for CrO_x/Cu-Ni and Pt/C respectively. The small Tafel slope of CrO_x/Cu-Ni catalyst compared to those of reported catalysts (Supplementary Table 3) further confirms the outstanding HER catalytic activity of the hybrid catalyst.

An important parameter of the catalyst is the stability. To assess stability of the catalyst in neutral media for HER, we measured 1000 continuous cyclic voltammograms for CrO_x/Cu-Ni catalyst between -0.3 and 0 V *vs.* RHE. Curves before and after cycling are identical, indicating a stable catalyst (Fig. 6c). The SEM image of the sample taken after 1000 CV cycles also shows no significant morphology degradation (inset in Fig. 6c). We further exploit the stability of our CrO_x/Cu-Ni HER catalyst at neutral conditions by performing a stability test at a constant applied voltage of -0.1 V *vs.* RHE. The catalyst exhibited a current density higher than 30 mA/cm^2. More importantly, the catalysts show no degradation over a period of 24 h continuous operation (Fig. 6d), confirming their excellent stability.

Conclusions

In summary, we present here the design principles of highly active HER catalysts in neutral media. High performance HER catalysts in this regime are of key importance to allow compatibility with biological processes capable of upgrading CO_2 into value-added chemicals. However, hydrogen evolution entails in this case an additional step and this dramatically hinders the efficiency of the process. Importantly, our design strategy only involves Earth-abundant and inexpensive materials. We found that the anisotropic doping of a metal surface can be used to asymmetrically destabilize bonds in the water molecule favouring its dissociation into H$^+$ and OH$^-$, which later react in metal surface to produce H$_2$. Based on our findings we fabricated a catalyst consisting of a Cu surface modified with Ni atoms and CrO_x clusters such that hydride coupling is significantly promoted reducing the energy barrier for water dissociation. This catalyst shows an exceptional performance, with a 48 mV overpotential at a current density of 10 mA·cm^{-2} in a pH 7 buffer electrolyte. Our findings open the door to the realization of inexpensive, efficient and biocompatible systems for energy storage and conversion and direct seawater splitting.

Methods

Deposition of transition metal oxides on Cu surface:

Metal oxide (MO_x, M = Cr, Al, Fe, Co, Ni, Ti, W) clusters were deposited on Cu surface using a thermodecomposition method. Typically, metal nitrate salts (Cr, Al, Fe, Co, and Ni) or metal alkoxide (Ti, W) were dissolved in ethanol with a concentration of 0.01 M. Next, 20 µl of metal precursor solution was spread on a surface of polished Cu foil (1 cm^2) and was dried at ambient conditions. The obtained metal precursors/Cu substrates were then heated at 400°C for 3 h in nitrogen atmosphere to form MO_x/Cu samples.

The 3D Cu nanowire network was prepared using a Cu foam substrate. First, Cu nanowire/Cu foam was obtained by heating the Cu foam at 550°C in air for 5 hours. The CuO nanowires were reduce to metallic Cu using an electrochemical method: CuO nanowires/Cu foam was used as a cathode and a constant current density of -10 mA/cm^2 was applied in a buffer solution (KH_2PO_4 + K_2HPO_4, pH 7). Ni and CrO_x were then subsequently deposited on 3D Cu nanowire scaffold using thermodepostion of nitrate salts as described above.

Materials characterization:

The morphology of the prepared electrodes were investigated using Scanning Electron Microscopy (SEM) on a Hitachi SU-8230 apparatus and Transmission Electron Microscopy (TEM) on a Hitachi HF-3300 instrument with an acceleration voltage of 200 kV. The oxidation state and compositions of the samples were studied by X-ray photoelectron spectroscopy (XPS) (model 5600, Perkin-Elmer). The binding energy data were calibrated with reference to the C 1s signal at 284.5 eV.

Ambient-pressure X-ray photoelectron spectroscopy studies were performed at the Advanced Light Source in Berkeley, at beam-line 9.3.2. AVG-Scienta R4000 HiPP analyzer was used[24]. The O 1s region was probed with a photon energy of 750 eV and an energy resolution of 0.1 eV. The Ni 3s region was probed with a photon energy of 420 eV. The calibration of the BE scale was carried out using the Au 4f photoelectron peak as reference (4f7/2 BE=84.0 eV), from a clean gold polycrystalline surface. The XPS peak shapes were fitted with CASAxps software using a Shirley background.

X-ray absorption spectroscopy (XAS) measurements at the Ni K-, Cr K- and Cu K-edges were carried out at the 9BM beamline of the Advanced Photon Source (APS, Argonne National Laboratory, IL) with an energy resolution of $\Delta E / E = 1 \times 10^{-4}$. Fluorescence yield signals were recorded in air using a solid state detector. XAS data was analyzed using the IFEFFIT package, in which energy calibration to respective metal foils and spectral normalization were performed using Athena software. A cubic spline function was used to fit the background above the absorption edge. For extended X-ray absorption fine structure (EXAFS) analysis, a k^2 weighting was applied to amplify the EXAFS oscillations in the mid-k region. Then a Fourier transform process was conducted to convert data to a radial distribution (R) space with a k range of $2.5 – 12$ Å^{-1} at the Cu K-edge and a k range of $2.5 – 12.5$ Å^{-1} at both Ni K- and Cr K-edges.

Electrochemical measurements:

Electrochemical measurements were performed using a three-electrode system connected to an electrochemical workstation (Autolab PGSTAT302N). For cyclic voltammetry analysis and linear sweep experiments, three-electrode chemistry was performed in a two-compartment H-cell using a Pt-foil counter electrode (with an area of 2 cm^2) and an

Ag/AgCl (3 M KCl) reference electrode at ambient condition. The area of the working electrode was 1 cm^2. The electrolytes for both anode and cathode were a pH 7 buffer solution (1 M KH$_2$PO$_4$ + K$_2$HPO$_4$) and were separated by a cation exchange membrane. All potentials were converted to RHE potential by using E$_{RHE}$ = E$_{Ag/AgCl}$ + 0.197 + 0.059×pH.

To measure the electrochemically active surface areas (ECSA), we employed the double layer capacitance formulation to compare the active surface area of our prepared electrocatalysts. The capacitance was measured using cyclic voltammetry with a scan rate in the range from 0.002 to 0.2 V/s in a non-Faradaic potential window of -0.7 to -0.6 V vs. Ag/AgCl in 1 M Ki buffer solution.

DFT calculations:

All DFT calculations were performed using the projected augmented wave pseudopotentials[26,27] and Perdew-Burke-Ernzerhof generalized gradient exchange approximation correlational functional[28] as implemented in computational package VASP[29]. Calculations were performed with planewave basis using a planewave kinetic energy cutoff of 400 eV and gamma-centered Monkhorst-Pack[30] electronic wavevector grid of 2×2×1. Spin-polarizations were included in all calculations and first order Methfessel-Paxton electron smearing of 0.05 eV was used. Hubbard correction were included using the rotationally invariant approach of Dudarev et al.[31] with a U value of 6.2 and 3.7 for Ni and Cr respectively[32]. Structures were considered relaxed when change in total energy of system was less than 1 meV.

Different surfaces were created by starting from a bulk-relaxed structure of Cu. First a 64 atoms, 4-layeryed, (111) slab of Cu is created was created. The bottom two layers of the slab was fixed at

bulk lattice constant and top two layered were allowed to relax. Ni-doped surface is created by changing one Cu atom from the top layer with Ni atom. For Cr_2O_3 deposited surface, we started with Cu surface and deposited 2 units of Cr_2O_3 (4 Cr atoms and 6 O atoms) on the top surface. All Cr and O atoms, along with top two layers of Cu surface were then relaxed until convergence was reached.

To calculate transition barriers, we first deposited a H_2O molecule on the catalyst surface and allowed it to relax to find the most stable site. We started with multiple initial configurations and selected the one with minimum energy (stable site close to the Cu/Cr_2O_3 interface in case of Cr_2O_3 deposited surface). Then, we find the multiple possible final locations of H^+ and OH^- on the surface and allowed each of these configurations to relax. We performed climbing image nudge elastic band calculations[33] on each of these combinations of final H + OH configuration with most stable initial H_2O configuration and selected the combination with least energy barrier for each surface. We calculate H-deadsorption energy as:

$$E_{desorption} = E[(H + OH)^*] - E[(OH)^*] - 0.5E(H_2),$$

Where $E[(X)^*]$ denotes energy of X adsorbed on surface and $E(H_2)$ is the energy of hydrogen molecule in gas phase.

Binding energies of H, OH, and H_2O are calculated as:

$$\Delta E_H^b = E[(H)^*] - E[*] - 0.5E(H_2)$$

$$\Delta E_{H_2O}^b = E[(H_2O)^*] - E[*] - E(H_2O)$$

$$\Delta E_{OH}^b = E[(OH)^*] - E[*] - E(H_2O) + 0.5E(H_2),$$

Where $E[(H)^*], E[(OH)^*]$, and $E[(H_2O)^*]$ are the energies of H, OH, and H_2O adsorbed on the catalyst surface. We note that, for consistency, we used the same surface sites here as those used in transition state barrier calculations. $E(H_2O)$ is the energy of H_2O molecule in gaseous phase.

Competing interests

The authors declare non-competing interests

Data availability

The data that support the plots within this paper and other findings of this study are available from the corresponding author upon reasonable request.

References

1   Turner, J. A. Sustainable hydrogen production. *Science* **305**, 972-974 (2014).

2   Luo, J. *et al.* Water photolysis at 12.3% efficiency via perovskite photovoltaics and Earth-abundant catalysts. *Science* **345**, 1593-1596 (2014).

3   Zhang, B. *et al.* Homogeneously dispersed multimetal oxygen-evolving catalysts. *Science* **352**, 333-337 (2016).

4   Zhao, S. *et al.* Ultrathin metal–organic framework nanosheets for electrocatalytic oxygen evolution. *Nat. Energy* **1**, 16184 (2016).

5   Zheng, Y. *et al.* High electrocatalytic hydrogen evolution activity of an anomalous ruthenium catalyst. *J. Am. Chem. Soc.* **138**, 16174–16181 (2016).

6   Strmcnik, D., Lopes, P. P., Genorio, B., Stamenkovic, V. R. & Markovic, N. M. Design principles for hydrogen evolution reaction catalyst materials. *Nano Energy* **29**, 29-36 (2016).

7   Subbaraman, R. *et al.* Trends in activity for the water electrolyser reactions on 3d M (Ni, Co, Fe, Mn) hydr (oxy) oxide catalysts. *Nat. Mater.* **11**, 550-557 (2012).

8   Subbaraman, R. *et al.* Enhancing hydrogen evolution activity in water splitting by tailoring Li^+-Ni $(OH)_2$-Pt interfaces. *Science* **334**, 1256-1260 (2011).

9   Miao, J. *et al.* Hierarchical Ni-Mo-S nanosheets on carbon fiber cloth: A flexible electrode for efficient hydrogen generation in neutral electrolyte. *Sci. adv.* **1**, e1500259 (2015).

10   Staszak-Jirkovský, J. *et al.* Design of active and stable Co-Mo-Sx chalcogels as pH-universal catalysts for the hydrogen evolution reaction. *Nat. Mater.* **15**, 197-203 (2016).

11   Nichols, E. M. *et al.* Hybrid bioinorganic approach to solar-to-chemical conversion. *Proc. Natl. Acad. Sci. USA* **112**, 11461-11466 (2015).

12   Liu, C., Colón, B. C., Ziesack, M., Silver, P. A. & Nocera, D. G. Water splitting–biosynthetic system with CO_2 reduction efficiencies exceeding photosynthesis. *Science* **352**, 1210-1213 (2016).

13   Torella, J. P. *et al.* Efficient solar-to-fuels production from a hybrid microbial–water-splitting catalyst system. *Proc. Natl. Acad. Sci. USA* **112**, 2337-2342 (2015).

14   Mudiyanselage, K. *et al.* Importance of the metal–oxide interface in catalysis: In situ studies of the water–gas shift reaction by ambient- pressure X- ray photoelectron spectroscopy. *Angew. Chem. Int. Ed.* **52**, 5101-5105 (2013).

15   Rodriguez, J. *et al.* Activity of CeO_x and TiO_x nanoparticles grown on Au (111) in the water-gas shift reaction. *Science* **318**, 1757-1760 (2007).

16   Henderson, M. A. The interaction of water with solid surfaces: fundamental aspects revisited. *Surf. Sci. Rep.* **46**, 1-308 (2002).

17   Huang, W. *et al.* Highly active and durable methanol oxidation electrocatalyst based on the synergy of platinum–nickel hydroxide–graphene. *Nat. Commun.* **6**, 10035 (2015).

18   Yin, H. *et al.* Ultrathin platinum nanowires grown on single-layered nickel hydroxide with high hydrogen evolution activity. *Nat. Commun.* **6**, 6430 (2015).

19   Gong, M. *et al.* Blending Cr_2O_3 into a NiO–Ni electrocatalyst for sustained water splitting. *Angew. Chem. Int. Ed.* **54**, 11989-11993 (2015).

20   Greeley, J., Jaramillo, T. F., Bonde, J., Chorkendorff, I. & Nørskov, J. K. Computational high-throughput screening of electrocatalytic materials for hydrogen evolution. *Nat. Mater.* **5**, 909-913 (2006).

21   Park, D., Yun, Y.-S. & Park, J. M. XAS and XPS studies on chromium-binding groups of biomaterial during Cr(VI) biosorption. *J. Colloid Interface Sci.* **317**, 54-61 (2008).

22   Anspoks, A. & Kuzmin, A. Interpretation of the Ni K-edge EXAFS in nanocrystalline nickel oxide using molecular dynamics simulations. *J. Non-Cryst. Solids* **357**, 2604-2610 (2011).

23   Grundner, S. *et al.* Single-site trinuclear copper oxygen clusters in mordenite for selective conversion of methane to methanol. *Nat. Commun.* **6**, 7546 (2015).

24   Grass, M. E. *et al.* New ambient pressure photoemission endstation at Advanced Light Source beamline 9.3.2. *Rev. Sci. Instrum.* **81**, 053106 (2010).

25   Callejas, J. F. *et al.* Electrocatalytic and photocatalytic hydrogen production from acidic and neutral-pH aqueous solutions using iron phosphide nanoparticles. *ACS nano* **8**, 11101-11107 (2014).

26   Blöchl, P. E. Projector augmented-wave method. *Phys. rev. B* **50**, 17953 (1994).

27   Kresse, G. & Joubert, D. From ultrasoft pseudopotentials to the projector augmented-wave method. *Phys. Rev. B* **59**, 1758 (1999).

28   Perdew, J. P., Burke, K. & Ernzerhof, M. Generalized gradient approximation made simple. *Phys. rev. lett.* **77**, 3865 (1996).

29   Kresse, G. & Hafner, J. *Ab initio* molecular dynamics for liquid metals. *Phys. rev. B* **47,** 558 (1993).

30   Monkhorst, H. J. & Pack, J. D. Special points for Brillouin-zone integrations. *Phys. rev. B* **13**, 5188 (1976).

31   Dudarev, S. L., Botton, G. A., Savrasov, S. Y., Humphreys, C. J. & Sutton, A. P. Electron-energy-loss spectra and the stability of nickel oxide: An LSDA+U study. *Phys. rev. B* **57**, 1505 (1998).

32   Jain, A. *et al.* Formation enthalpies by mixing GGA and GGA+U calculations. *Phys. rev. B* **84**, 045115 (2011).

33   Henkelman, G., Uberuaga, B. P. & Jónsson, H. A climbing image nudged elastic band method for finding saddle points and minimum energy paths, *J. Chem. Phys.* **113**, 9901 (2000).

Acknowledgements

Author contributions

E.H.S. supervised the project. C. T. D. and F. P. G. A designed and carried out the experiments. A. J. carried out the DFT calculation. J. C., B. Z. G and E. J. C. performed the APXPS measurements. J. L performed the XAS measurements. C. T. D., A. J., F. P. G. A. and E. H. S. wrote the manuscript. All the authors discussed the results and assisted during the manuscript preparation.
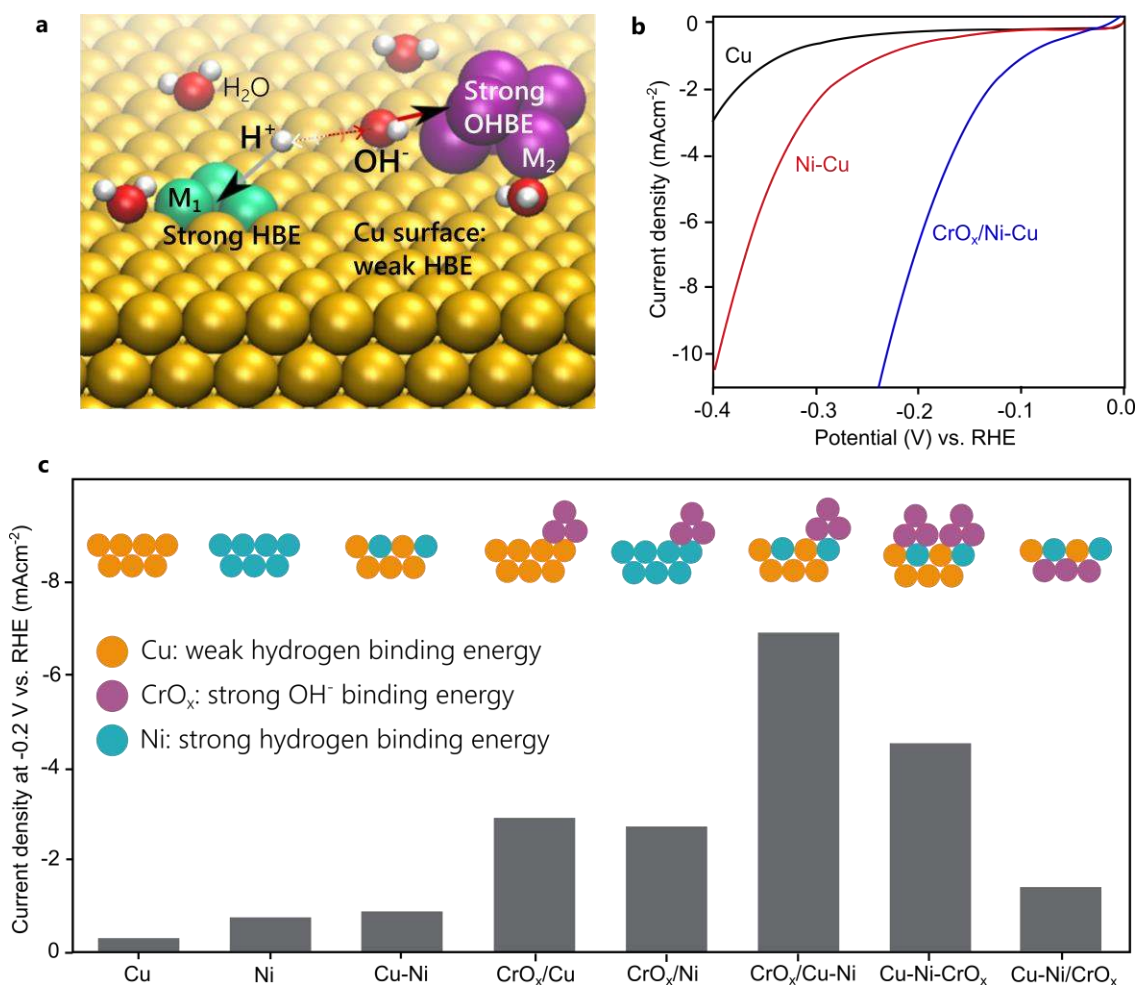
Figure 1 │ Catalyst design principle and HER activities of CrO$_x$/Cu-Ni Catalyst. (a) Design principle of HER catalysts in neutral water by anisotropic surface doping to destabilize the water molecule on catalyst surface. Metal sites M$_1$ (turquoise color-coded) with a strong hydrogen binding energy (HBE) and M$_2$ (purple) with a strong OH$^-$ affinity are doped onto a Cu substrate (orange) with a weak HBE. (b) Representative *J-V* curves before *iR* correction show a significant improvement on HER activity of CrO$_x$/Cu-Ni compared to pure Cu or Cu-Ni alloy catalysts. (c) Comparison of the HER activities on various Cu-Ni-CrO$_x$ catalysts shows the optimal CrO$_x$/Cu-Ni structure with highest catalytic activity. The insets represent the catalyst configuration, which comprises a substrate (bottom) and two types of dopants (substitutional or adatom).
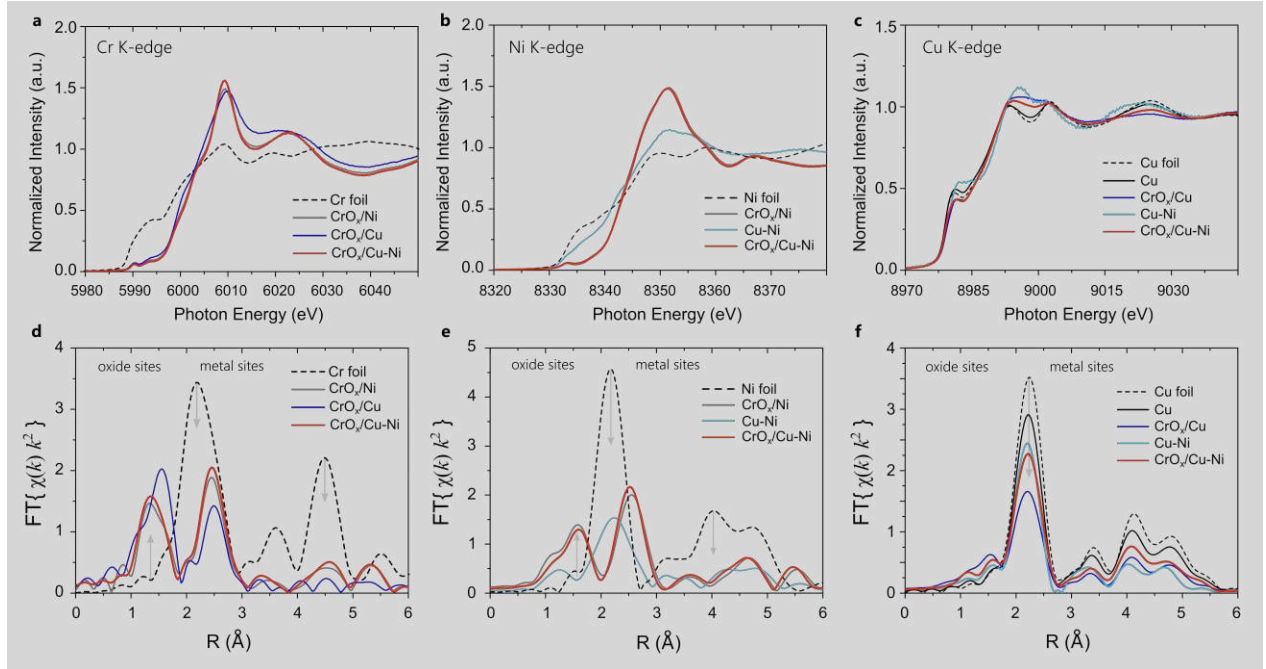
Figure 2 │ CrOₓ/Cu-Ni catalyst fine structures revealed by X-ray absorption spectroscopies.
(a-c) X-ray absorption and (d-f) Fourier analysis of the extended X-ray absorption fine structures (EXAFS) of CrOₓ/Cu-Ni samples and controls at the Cr, Ni and Cu K-edges in fluorescence mode showing the effect of CrOₓ on the oxidation state and local environment of Ni and Cu. A k^2 weighting was applied to amplify the EXAFS oscillations in the mid-k region. This was converted back to the radial distribution (R) space with a k range of $2.5 - 12$ Å⁻¹ for the Cu K-edge and with a range of $2.5 - 12.5$ Å⁻¹ for both Ni K- and Cr K-edges. The arrows indicate the trend compared to reference sample. All measurements were taken under vacuum.
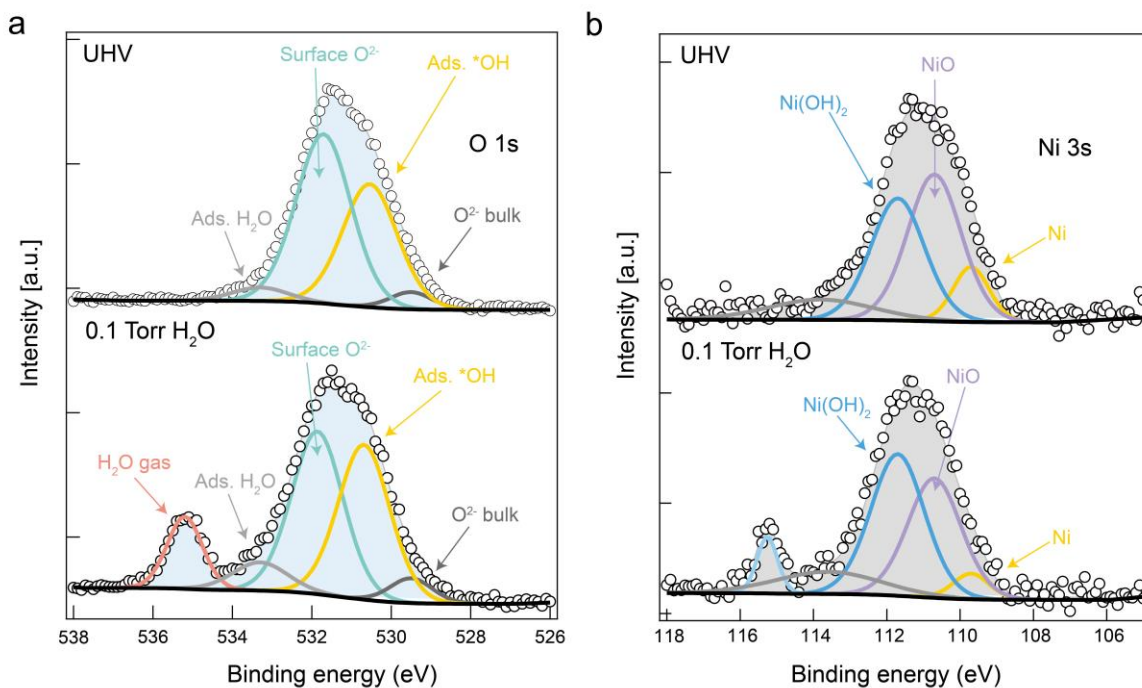
Figure 3 │ Ambient pressure XPS experiments of water adsorption on CrO_x/Cu-Ni. (a) O 1s of CrO_x/Cu-Ni under ultrahigh vacuum (UHV) and 0.1 Torr of H_2O pressure showing the increase of adsorbed $^*OH$ surface under water pressure as a result of water dissociation process. The surface O^{2-} species are attributed to surface CO_3^{2-} and C-OH. (b) Ni 3s XPS spectra for CrO_x/Cu-Ni under UHV and 0.1 Torr of water pressure showing the change from Ni surface to $Ni(OH)_2$ surface in the presence of water vapor. All spectra were normalised to facilitate comparison. The peaks at 114 eV in the Ni 3s spectra are satellites. The peak shapes were fitted with CASA XPS software using a Shirley background.
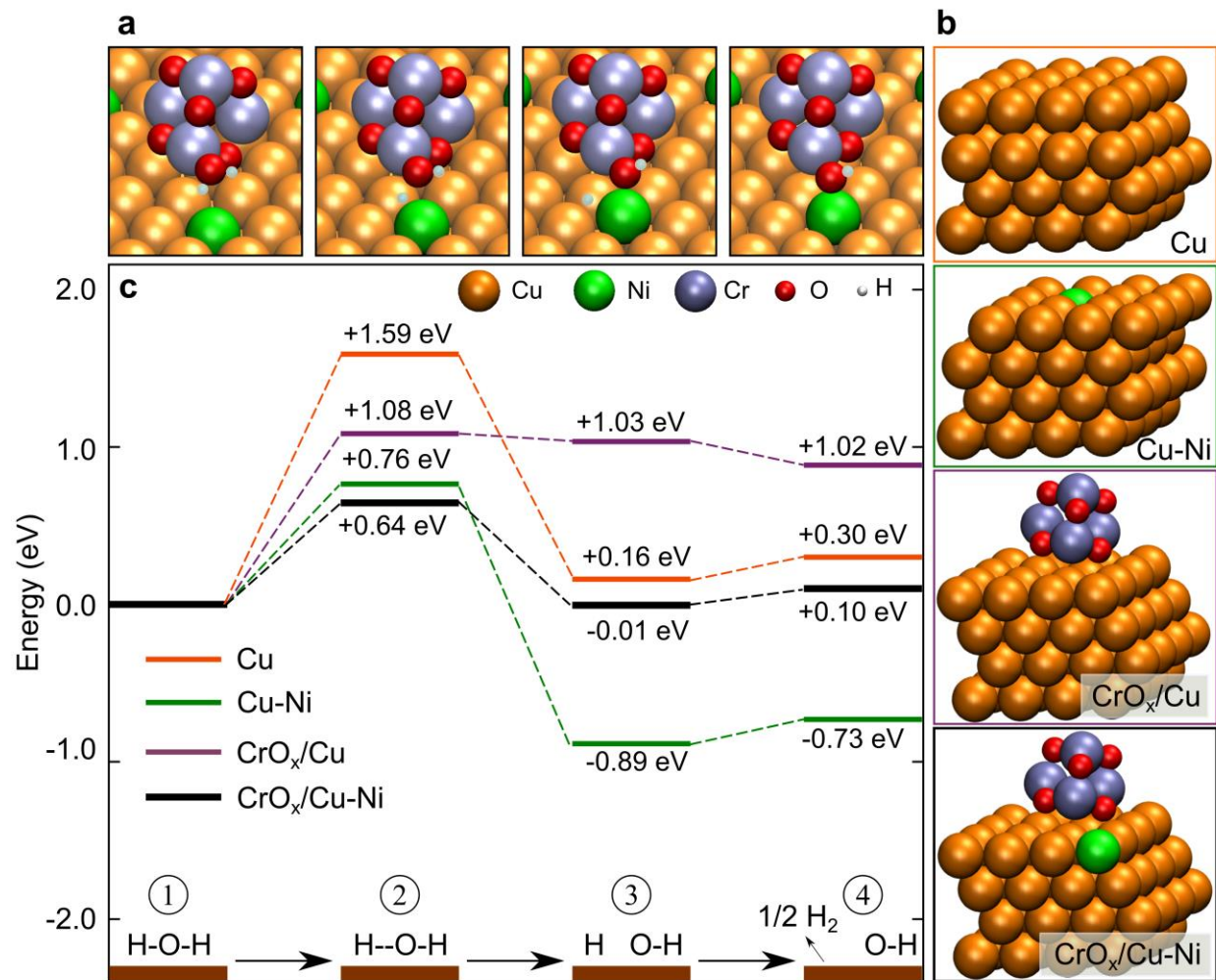
Figure 4 | Theoretical calculation of HER activation energy on CrO$_x$/Cu-Ni catalysts. $\Delta E_{2\text{-}1}$ and $\Delta E_{4\text{-}3}$ are the related kinetic energy barriers for water dissociation and H$_2$ formation on the surface of the catalysts, respectively. E (eV) in the diagram represents the free energies of the different stages of the reaction in which CrO$_x$/Cu-Ni show the lowest energy barrier. (top panel) surface configurations of CrO$_x$/Cu-Ni at different stages of the reaction. (right panel) surface configuration of the four different catalysts used for the calculation (Cu, Cu-Ni, CrO$_x$/Cu and CrO$_x$/Cu-Ni).
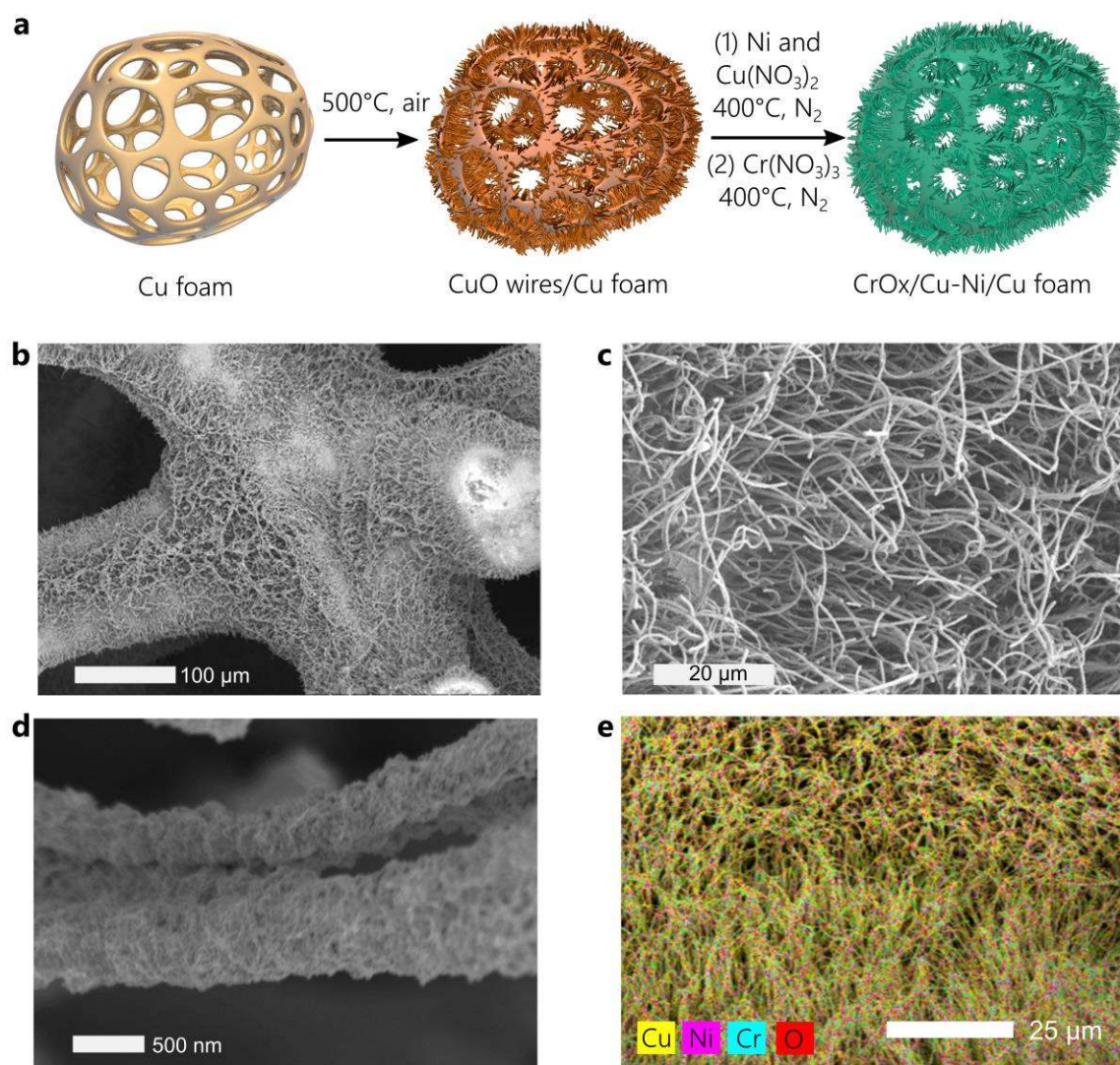
Figure 5 │ Design and characterization of 3D CrO$_x$/Cu-Ni catalyst. (a) Schematic illustration of the preparation pathway for 3D CrO$_x$/Cu-Ni from Cu foam as a substrate followed by the growing of CuO nanowire and coating of CrO$_x$/Cu-Ni active phase. (b-d) SEM images at different magnification and (e) elemental EDX mapping for CrO$_x$/Cu-Ni deposited on 3D Cu nanowire structure.
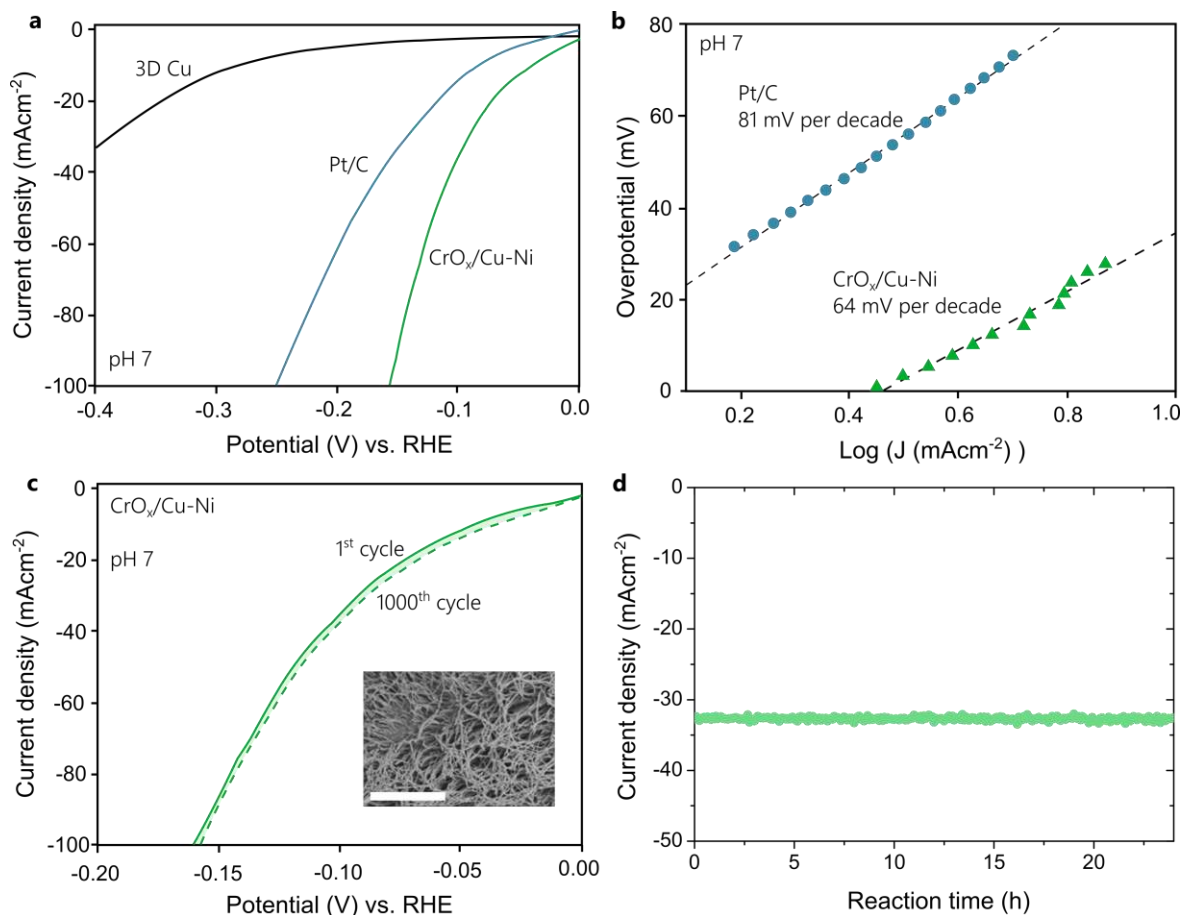
Figure 6 │ Electrochemical characterization of CrO_x/Cu-Ni on 3D Cu foam │ (a) *J–V* curves after *iR* correction show the catalytic performance of the CrO_x/Cu-Ni in comparison to a Pt/C and 3D Cu foam in buffer solution of 1M KPi. (b) Tafel plots of the CrO_x/Cu-Ni and Pt/C catalysts recorded in a. (c) *J-V* curves showing negligible current density loss of CrO_x/Cu-Ni catalyst initially and after 1,000 CV cycles. Inset: SEM of the sample after 1000th cycles operation. Scale bar is 10 μm (d) Time dependence of current density for the CrO_x/Cu-Ni HER cathode reaction at a fixed -100 mV potential.